

A new polarization amplitude bias reduction method

DOI:

[10.1093/mnras/stw1298](https://doi.org/10.1093/mnras/stw1298)

Document Version

Accepted author manuscript

[Link to publication record in Manchester Research Explorer](#)

Citation for published version (APA):

Vidal Navarro, M. A., Leahy, J. P., & Dickinson, C. (2016). A new polarization amplitude bias reduction method. *Monthly Notices of the Royal Astronomical Society*, 461(1), 698-709. <https://doi.org/10.1093/mnras/stw1298>

Published in:

Monthly Notices of the Royal Astronomical Society

Citing this paper

Please note that where the full-text provided on Manchester Research Explorer is the Author Accepted Manuscript or Proof version this may differ from the final Published version. If citing, it is advised that you check and use the publisher's definitive version.

General rights

Copyright and moral rights for the publications made accessible in the Research Explorer are retained by the authors and/or other copyright owners and it is a condition of accessing publications that users recognise and abide by the legal requirements associated with these rights.

Takedown policy

If you believe that this document breaches copyright please refer to the University of Manchester's Takedown Procedures [<http://man.ac.uk/04Y6Bo>] or contact uml.scholarlycommunications@manchester.ac.uk providing relevant details, so we can investigate your claim.



A new polarisation amplitude bias reduction method.

M. Vidal^{1,2*}, J. P. Leahy^{1†} and C. Dickinson^{1‡}

¹*Jodrell Bank Centre for Astrophysics, Alan Turing Building, School of Physics and Astronomy, The University of Manchester, Oxford Road, Manchester M13 9PL, U.K.*

²*Departamento de Astronomía, Universidad de Chile, Casilla 36-D, Santiago, Chile.*

31 May 2016

ABSTRACT

Polarisation amplitude estimation is affected by a positive noise bias, particularly important in regions with low signal-to-noise ratio (SNR). We present a new approach to correct for this bias in the case there is additional information about the polarisation angle. We develop the ‘known-angle estimator’ that works in the special case when there is an independent and high signal-to-noise ratio ($\gtrsim 2\sigma$) measurement of the polarisation angle. It is derived for the general case where the uncertainties in the Q, U Stokes parameters are not symmetric. This estimator completely corrects for the polarisation bias if the polarisation angle is perfectly known. In the realistic case, where the angle template has uncertainties, a small residual bias remains, but that is shown to be much smaller than the one left by other classical estimators. We also test our method with more realistic data, using the noise properties of the three lower frequency maps of *WMAP*. In this case, the known-angle estimator also produces better results than methods that do not include the angle information. This estimator is therefore useful in the case where the polarisation angle is expected to be constant over different data sets with different SNR.

Key words: polarisation – techniques: polarimetric – methods: data analysis – methods: statistical – radiation mechanisms: non-thermal

1 INTRODUCTION

It has long been noticed that observations of linear polarisation are subject to a positive bias (Serkowski 1958). Given the positive nature of the polarisation amplitude, $P = \sqrt{Q^2 + U^2}$, even if the true Stokes parameters Q_0, U_0 are zero, P will yield a non-zero estimate in the presence of noise. The effect is particularly important in the low signal-to-noise ratio (SNR) regime. Ways to correct for the bias have been studied in detail for the special case where the uncertainties for (Q, U) are equal and normally distributed around their true value (Q_0, U_0) (Wardle & Kronberg 1974; Simmons & Stewart 1985; Vaillancourt 2006; Quinn 2012). Montier et al. (2015a,b) give a useful review comparing different bias reduction methods.

In this paper we propose a new approach, useful when there is an independent measurement of the polarisation angle $\chi = 0.5 \arctan(U/Q)$. This situation occurs, for instance, in the polarisation datasets from *WMAP* (Bennett et al. 2013) and *Planck* (Planck Collaboration et al. 2014), where over a range of frequency the polarisation angle is expected to be nearly constant (e.g. synchrotron radiation will have the same polarisation angle at different frequencies as this angle depends on the direction of the magnetic field of

the emitting medium), and the variation of the polarised intensity with frequency is of interest. Using simulations, we test the performance of this estimator compared to previous methods from the literature that do not include angle information. In Section 2 we show the origin of the bias and we describe some methods used to correct for it. In Section 3 we derive our new estimator, its uncertainty and residual bias. In Section 4 we use simulations to test its performance. Section 5 concludes.

2 BIAS CORRECTION METHODS

We will first review the simple case when the uncertainties in Q and U are equal, and then study the more general case with asymmetric uncertainties.

2.1 Symmetric uncertainties

Let us take (Q_0, U_0) as the true Stokes parameters from a source and (Q', U') the measured ones. We can write the joint probability distribution function (p.d.f.) for (Q', U') as the product of the individual normal distributions

$$f(Q', U') = \frac{1}{2\pi\sigma^2} \exp\left[-\frac{(Q' - Q_0)^2 + (U' - U_0)^2}{2\sigma^2}\right], \quad (1)$$

where $\sigma_Q = \sigma_U = \sigma$ is the uncertainty in Q' and U' .

* E-mail: mvidal@das.uchile.cl

† E-mail: j.p.leahy@manchester.ac.uk

‡ E-mail: clive.dickinson@manchester.ac.uk

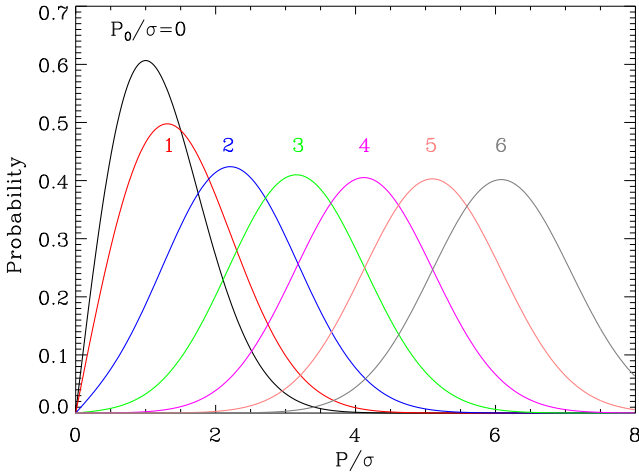


Figure 1. Rice distribution (Eq. 3) plotted for different values of the true SNR, P_0/σ . The asymmetry and bias are clear in the low SNR level. At high SNR, the distribution converges to a Gaussian with standard deviation σ centred at $\sqrt{P_0 + \sigma^2}$.

Transforming into polar coordinates using the definitions for the polarisation amplitude $P = \sqrt{Q^2 + U^2}$ and the polarisation angle $\chi = \frac{1}{2} \arctan(U/Q)$, we have:

$$\begin{aligned} f(P', \chi') &= \frac{P'}{\pi\sigma^2} e^{-[P'^2 + P_0^2 - 2(P' \cos 2\chi' P_0 \cos 2\chi_0 + P \sin 2\chi' P_0 \sin 2\chi_0)]/2\sigma^2} \\ &= \frac{P'}{\pi\sigma^2} e^{-(P'^2 + P_0^2)/2\sigma^2} e^{-P' P_0 \cos[2(\chi' - \chi_0)]/\sigma^2}. \end{aligned} \quad (2)$$

The marginal probability distribution for P' is obtained by integrating $f(P', \chi')$ over χ' . This angular integral can be written as a function of the modified Bessel function of first type $I_0(z)$, yielding the Rice distribution for polarisation (Rice 1945):

$$R(P'|P_0) = \frac{P'}{\sigma^2} I_0\left(\frac{P' P_0}{\sigma^2}\right) e^{-(P'^2 + P_0^2)/2\sigma^2}. \quad (3)$$

It is important to note that the integral of $R(P'|P_0)$ represents the probability of measuring P' inside an interval for a given true polarisation P_0 . Fig. 1 shows $R(P'|P_0)$ for different SNR. The bias, defined as $\langle P' \rangle - P_0$, arises because this probability distribution is not symmetric, and becomes clear in Fig. 1 at low SNR. Even when the true SNR is zero (black curve in the figure), the measured value is close to 1. At large SNR, the distribution approaches a Gaussian with mean close to P_0 and standard deviation close to σ .

Simmons & Stewart (1985) compared five estimators for P_0 (including the uncorrected P'), and concluded that the one with smallest residual bias when $P_0/\sigma \gtrsim 0.7$ is that suggested by Wardle & Kronberg (1974):

$$\left. \frac{\partial R}{\partial P'}(P', P_0) \right|_{P_0 = \hat{P}} = 0. \quad (4)$$

(note that this is *not* the maximum likelihood estimator). Even at moderate SNR, the rice distribution is not centred at the measured SNR, this can be seen in Fig. 1, where the distributions have mean $\sqrt{P_0 + \sigma^2}$. This motivated Wardle & Kronberg (1974) to propose a very simple estimator

$$\hat{P}_{AS} = \begin{cases} \sqrt{P'^2 - \sigma^2} & P' \geq \sigma; \\ 0 & \text{otherwise.} \end{cases} \quad (5)$$

This approximates Eq. 4, and also has the virtue of giving lower

bias at very low SNR, albeit at the cost of a 1 per cent over-correction near SNR = 2; this has been widely used in practice. Montier et al. (2015b) compared various estimators of the polarisation angle in terms of the residual bias, risk, variance and Gaussianity. An unwanted property of the asymptotic (AS, Eq. 5) estimator is that the distribution of the estimator is discontinuous as it yields zeroes below a particular SNR (see Eq. 5). It is illuminating to re-write Eq. 5 in terms of the error in the polarisation angle, $\sigma_\chi = \sigma/2P'$, so

$$\hat{P}_{AS} = P' \sqrt{1 - 4\sigma_\chi^2}. \quad (6)$$

This emphasises that the source of the bias is the error in the angle of the (Q, U) vector, which contributes a component of the error vector orthogonal to the true polarisation with length $P' \sin 2\Delta\chi$, and is added in quadrature to the parallel component, hence always contributing a positive bias.

For the polarisation angle, here we use the naive estimator, $\chi = \frac{1}{2} \arctan(U/Q)$, which is completely unbiased. The uncertainty of this estimator, on the asymptotic case where $P_0 \gg \sigma$ is (Vinokur 1965; Montier et al. 2015a)

$$\sigma_\chi = \sqrt{Q'^2 \sigma_Q^2 + U'^2 \sigma_U^2} / 2P^2. \quad (7)$$

2.2 Asymmetric uncertainties

The previous case in which the uncertainties in (Q', U') are equal and uncorrelated is well understood. The asymmetric case is interesting as many polarisation data sets have this characteristic. For example, the CMB experiments *WMAP* (Bennett et al. 2013) and *Planck* (Planck Collaboration et al. 2014) have correlations between the (Q', U') uncertainties due to non-uniform azimuthal coverage for each pixel in the sky. This case has been recently studied by Montier et al. (2015a,b); Plaszczyński et al. (2014). The error distribution in these cases is an elliptical 2D Gaussian in (Q', U') , characterised by a covariance matrix (e.g. Kendal, Stuart & Ord 1994)

$$C = \begin{pmatrix} \sigma_Q^2 & \text{cov}_{QU} \\ \text{cov}_{QU} & \sigma_U^2 \end{pmatrix} \quad (8)$$

Defining a (Q, U) error vector

$$\delta = \begin{pmatrix} Q' - Q_0 \\ U' - U_0 \end{pmatrix}, \quad (9)$$

we have

$$\begin{aligned} f(Q', U') &= \frac{1}{2\pi\sqrt{\det[C]}} \exp\left[-\frac{\delta^T C^{-1} \delta}{2}\right] \\ &= \frac{1}{2\pi\sigma_Q\sigma_U\sqrt{1-\rho^2}} \exp\left[-\frac{1}{2(1-\rho^2)} \left(\frac{(Q' - Q_0)^2}{\sigma_Q^2} + \frac{(U' - U_0)^2}{\sigma_U^2} - \frac{2\rho(Q' - Q_0)(U' - U_0)}{\sigma_Q\sigma_U} \right)\right], \end{aligned} \quad (10)$$

where ρ is the correlation coefficient between (Q_0, U_0) ,

$$\rho = \frac{E[(Q' - Q_0)(U' - U_0)]}{\sigma_Q\sigma_U} = \frac{\text{cov}_{QU}}{\sigma_Q\sigma_U}. \quad (11)$$

The error ellipse in the Q, U plane will be rotated an angle θ in the

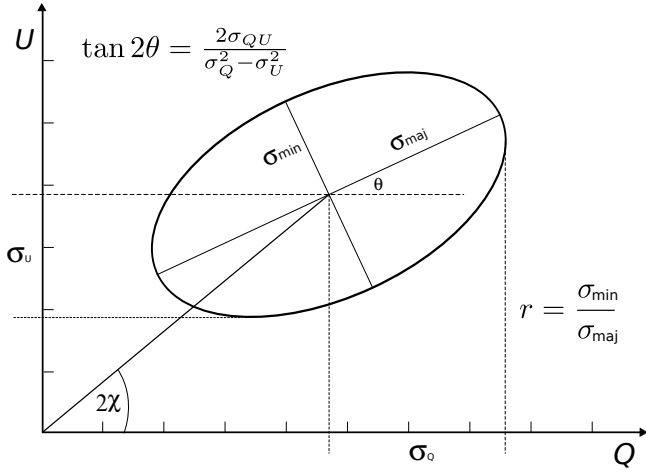


Figure 2. Error ellipse in the (Q, U) plane showing how the polarisation angle χ and the rotation angle θ are related.

case of a non-zero cov_{QU} (see Fig. 2). In terms of the components of the covariance matrix,

$$\theta = \frac{1}{2} \arctan \frac{2\text{cov}_{QU}}{\sigma_Q^2 - \sigma_U^2}. \quad (12)$$

The error ellipse has axial ratio

$$r = \frac{\sigma_{\min}}{\sigma_{\max}}, \quad (13)$$

where

$$\sigma_{\max}^2 = \frac{1}{2} \left(\sigma_Q^2 + \sigma_U^2 + \sqrt{(\sigma_Q^2 - \sigma_U^2)^2 + 4\text{cov}_{QU}^2} \right) \quad (14)$$

$$\sigma_{\min}^2 = \frac{1}{2} \left(\sigma_Q^2 + \sigma_U^2 - \sqrt{(\sigma_Q^2 - \sigma_U^2)^2 + 4\text{cov}_{QU}^2} \right). \quad (15)$$

Allowing for correlated variables, the error in any $f(Q', U')$ is to first order

$$\sigma_f^2 = \left(\frac{\partial f}{\partial Q'} \right)^2 \sigma_Q^2 + 2 \frac{\partial f}{\partial Q'} \frac{\partial f}{\partial U'} \text{cov}_{QU} + \left(\frac{\partial f}{\partial U'} \right)^2 \sigma_U^2. \quad (16)$$

Hence (Montier et al. 2015a),

$$\begin{aligned} \sigma_p^2 &= \frac{Q'^2 \sigma_Q^2 + 2Q'U' \text{cov}_{QU} + U'^2 \sigma_U^2}{p'^2} \\ &= \cos^2 2\chi' \sigma_Q^2 + 2 \cos 2\chi' \sin 2\chi' \text{cov}_{QU} + \sin^2 2\chi' \sigma_U^2 \end{aligned} \quad (17)$$

$$\sigma_\chi^2 = \frac{\sin^2 2\chi' \sigma_Q^2 - 2 \cos 2\chi' \sin 2\chi' \text{cov}_{QU} + \cos^2 2\chi' \sigma_U^2}{4p'^2}, \quad (18)$$

When $r \neq 1$, the polarisation bias depends on the polarisation angle χ_0 , more specifically on $\theta - 2\chi_0$, as well as on p_0 . The asymptotic estimator from Eq. 6, $\hat{p}_{AS} = P' \sqrt{1 - 4\sigma_\chi^2}$, still applies, provided we use the generalised form of σ_χ derived above. We note that Eq. 18 is derived in the small-error approximation and uses the observed polarisation angle, χ' as a surrogate for the true polarisation angle χ_0 , which is unobjectionable in the high SNR regime. When SNR is low it is not so obvious that this is appropriate, but we will verify by simulations that the estimator remains reasonably effective.

The preferred estimator of Montier et al. (2015b), is the ‘modified asymptotic estimator’, MAS (Płaszczynski et al. 2014), which using the above notation is given by:

$$\hat{p}_{MAS} = P' \left[1 - 2\sigma_\chi^2 \left(1 - e^{-P'^2/b^2} \right) \right], \quad (19)$$

3 KNOWN-ANGLE ESTIMATOR

As we will see, all estimators based exclusively on one observed (Q', U') measurement give a significant positive bias at very low SNR. However, this can be overcome if we have an independent estimate of the polarisation angle χ . We will refer to this as the ‘template’ observation, in contrast to the ‘target’ observation to be debiased.

We will build a new estimator, based on the maximum likelihood estimator, assuming that the true angle χ_0 is known. We will later calculate the residual bias which emerges because of uncertainty in our template angle, hereafter denoted χ , as distinct from the true angle χ_0 and the observed angle χ' from the target observation.

To find our known-angle estimator, \hat{p}_χ , we take the joint p.d.f. for the observed values (Q', U') with asymmetric uncertainties from Eq. 10. Since $Q_0 = P_0 \cos 2\chi_0$ and $U_0 = P_0 \sin 2\chi_0$,

$$f(Q', U') = \frac{1}{2\pi\sigma_Q\sigma_U\sqrt{1-\rho^2}} \exp \left[-\frac{1}{2(1-\rho^2)} \left(\frac{(Q' - P_0 \cos 2\chi_0)^2}{\sigma_Q^2} + \frac{(U' - P_0 \sin 2\chi_0)^2}{\sigma_U^2} - \frac{2\rho(Q' - P_0 \cos 2\chi_0)(U' - P_0 \sin 2\chi_0)}{\sigma_Q\sigma_U} \right) \right]. \quad (20)$$

The maximum likelihood estimator in this case, \hat{p}_χ , is defined by the condition:

$$\left. \frac{\partial f(Q', U')}{\partial P_0} \right|_{P_0=\hat{p}_\chi} = 0. \quad (21)$$

With the assumption that $\chi_0 = \chi$, this leads to the expression for the de-biased polarisation amplitude,

$$\hat{p}_\chi = \frac{\sigma_U^2 Q' \cos 2\chi - \text{cov}_{QU} (Q' \sin 2\chi + U' \cos 2\chi) + \sigma_Q^2 U' \sin 2\chi}{\sigma_U^2 \cos^2 2\chi - 2\text{cov}_{QU} \sin 2\chi \cos 2\chi + \sigma_Q^2 \sin^2 2\chi}. \quad (22)$$

We note that if the observed polarisation angle χ' is used as a surrogate for χ_0 , then $\hat{p}_\chi = p' = \sqrt{Q'^2 + U'^2}$ and there is no correction whatsoever – we do need an independent constraint on χ to benefit from this approach.

The error in \hat{p}_χ is given via Eq. 16:

$$\begin{aligned} \sigma_{\hat{p}_\chi}^2 &= \frac{\sigma_Q^2 \sigma_U^2 - \sigma_{QU}^2}{\sigma_U^2 \cos^2 2\chi - 2\text{cov}_{QU} \sin 2\chi \cos 2\chi + \sigma_Q^2 \sin^2 2\chi} \\ &= \frac{\det[C]}{4P'^2 \sigma_\chi^2}. \end{aligned} \quad (23)$$

The known-angle estimator still contains a residual bias, due to the uncertainty in the template angle χ . Specifically the expected value of the fractional bias is

$$b_\chi \equiv \frac{\langle \hat{p}_\chi \rangle - P_0}{P_0} = \int_\chi f(\chi|\chi_0) \int_{Q', U'} f(Q', U'|P_0, \chi_0) \frac{\hat{p}_\chi}{P_0} dQ' dU' - 1. \quad (24)$$

Since \hat{p}_χ is linear in $Q' = P_0 \cos 2\chi_0 + \delta_Q$ and in $U' = P_0 \sin 2\chi_0 + \delta_U$, integrating over the Gaussian probability distribution of (Q', U') eliminates the dependence on the deviations δ_Q , δ_U , and we have

$$b_\chi = \int_\chi f(\chi|\chi_0) \frac{\sigma_U^2 P_0 \cos 2\chi_0 \cos 2\chi - \text{cov}_{QU} P_0 (\cos 2\chi_0 \sin 2\chi + \sin 2\chi_0 \cos 2\chi) + \sigma_Q^2 P_0 \sin 2\chi_0 \sin 2\chi}{P_0 (\sigma_U^2 \cos^2 2\chi - 2\text{cov}_{QU} \cos 2\chi \sin 2\chi + \sigma_Q^2 \sin^2 2\chi)} d\chi - 1, \quad (25)$$

where $f(\chi|\chi_0)$ is the p.d.f. of the template angle.

The amplitude of the polarised signal, P_0 , cancels, so the residual bias just depends on the axial ratio of the (Q, U) error ellipse, r , and the difference between the orientation of the ellipse, θ , and that of the true (Q_0, U_0) vector, $2\chi_0$ (see Fig. 2). If the angle is known exactly so $f(\chi|\chi_0) = \delta(\chi - \chi_0)$, the residual bias vanishes.

In the special case where $\text{cov}_{QU} = 0$, so $r = \sigma_U/\sigma_Q$, we have

$$b_\chi = \int_\chi f(\chi|\chi_0) \frac{r^2 \cos 2\chi_0 \cos 2\chi + \sin 2\chi_0 \sin 2\chi}{r^2 \cos^2 2\chi + \sin^2 2\chi} d\chi - 1. \quad (26)$$

The top panel of Fig. 3 shows the bias for different axial ratios of the error ellipse as function of the polarisation angle (see the angle definitions in Fig. 2). Here the uncertainty in the template angle is Gaussian (c.f. Eq. 7) and it is fixed at $\sigma_\chi = 5^\circ$. If the error distribution is symmetric ($r = 1$), the bias is constant (cf. Eq. 26). The bottom panel of Fig. 3 shows the bias for different values of the uncertainty in the template angle, for an error ellipse with axial ratio $r = 0.5$. The bias is usually negative, i.e. the polarised intensity is slightly underestimated.

When the template for the angle has an SNR at least 2 times larger than the target, the known-angle estimator thus gives excellent performance at very low signal-to-noise levels, where other estimators have large residual biases. However, for a given uncertainty in χ , the bias does not decrease as the signal in (Q', U') rises, unlike all the standard estimators. In practical use, the estimator is only worthwhile when a template observation with substantially higher SNR than the target observations is available; fortunately, this situation is fairly common, as discussed in Section 4.3.

4 TESTS OF THE ESTIMATORS

Here we compare the effectiveness of three bias reduction methods using Monte Carlo simulations for a range of SNR. This is to show what can be gained when including additional angle information from a higher signal-to-noise template. In section 4.2 we study the residual bias in a single pixel for a range of SNR in (Q, U) . Section 4.3 tests the methods using real noise values from the *WMAP* polarisation data.

Using Monte Carlo simulations, we measure the residual bias in a single pixel for four polarisation amplitude estimators:

(i) $\hat{p}' = P' = \sqrt{Q'^2 + U'^2}$, the naive estimator with no correction for bias.

(ii) \hat{p}_{MAS} , the Plaszczyński et al. modified asymptotic estimator, from Eq. 19.

(iii) \hat{p}_χ , the known-angle estimator, from Eq. 22.

4.1 Isotropic case

We ran 10^6 Gaussian noise realisations for the Q, U Stokes parameters. For the known-angle estimator, we also produced an additional set of 10^6 noise realisations for the high signal-to-noise template Q, U , which accounts for the uncertainty in the known angle. We start with the simpler case where σ_Q and σ_U are not correlated. We studied the bias, defined as $\text{bias} = \hat{p} - P_0$ and the risk function

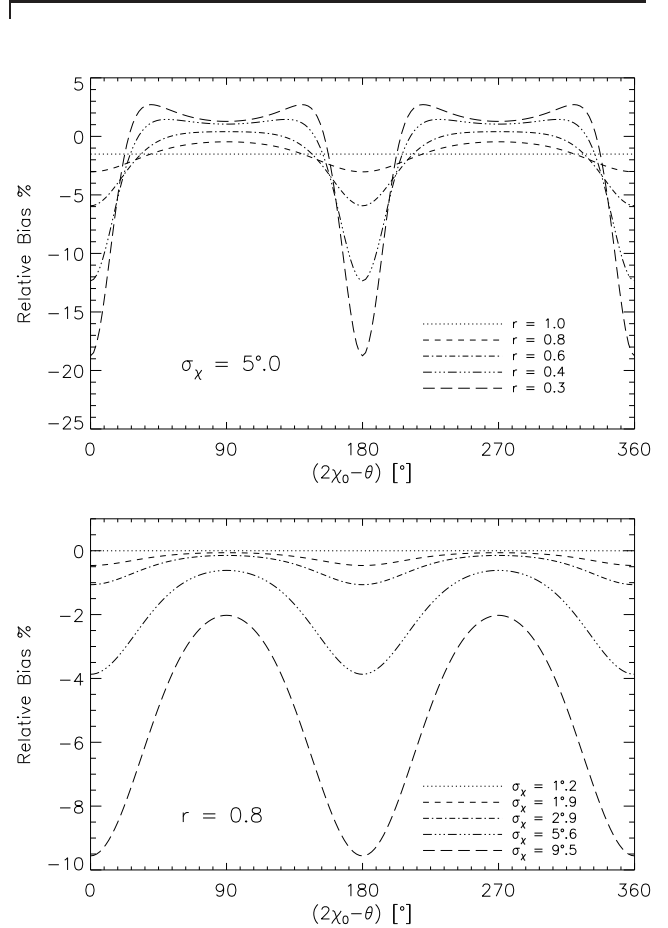


Figure 3. Fractional bias of the known-angle estimator, \hat{p}_χ , for different values of the error ellipse ($r = \sigma_U/\sigma_Q$) and an uncertainty in the template angle of 5° (top). The bottom plot shows the residual fractional bias of \hat{p}_χ for different values of the uncertainty in the template angle, σ_χ , for a fixed value of $r = 0.8$. Both plots are calculated with $P_0 = 1$.

$= \langle (\hat{p} - P_0)^2 \rangle$, for the different estimators. In Fig. 4 we show on the top panel the residual bias of the estimators as a function of the observed $\text{SNR}_P \equiv P_0/\sigma_P$, with σ_P defined in Eq. 17. We show four lines for \hat{p}_χ , which correspond to different values of the SNR of the angle template. The bottom panel of Fig. 4 shows the risk function for the different estimators.

We can see that the known-angle estimator performs very well in the case when the polarisation angle is known with relatively high precision, i.e. when the SNR of the template is > 2 – 3 times the SNR of the target.

The construction of the known-angle estimator allows for negative values of \hat{p}_χ . Fig. 5 shows the distributions of \hat{p}_χ simulations for three different values of the SNR of the target and the template.

4.2 General case

Here we allow for asymmetric errors in Q, U , i.e. for $r < 1$. We created a grid of 100×100 different values of Q_0/σ_Q and U_0/σ_Q , in

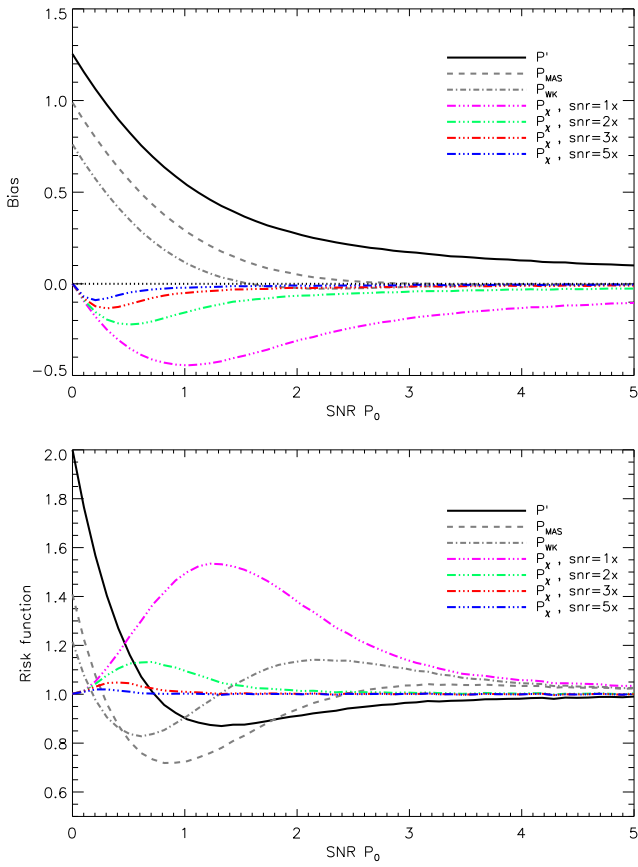


Figure 4. Residual bias (*top*) and risk function (*bottom*) for the naive, \hat{p}^i (continuum line), \hat{p}^{MAS} (dashed), \hat{p}^{AS} (dot-dashed line) and \hat{p}_χ (colours) estimators as a function of the SNR of the true polarisation amplitude P_0 . As the residual bias and risk function of the known-angle estimator depends on the uncertainty of the high SNR template, we show these two functions for four different values of the uncertainty of the high SNR template: same SNR of the target in magenta, 2 times the SNR of the target in green, 3 times in red and 5 times better in blue. Both plots are for the isotropic case, $\sigma_Q = \sigma_U$.

the range $Q_0/\sigma_Q \leq 4$, $U_0/\sigma_Q \leq 4$, using a uniform spacing. This was repeated for four values of r . We set $\theta = 0$, so that $r = \sigma_U/\sigma_Q$ (the pattern in the (Q, U) plane simply rotates for other values of θ). Then, $\times 10^5$ Gaussian noise realisations are added to the each point in the grid. We calculated the ‘observed’ polarisation amplitude P' from the noisy simulations, applied the four estimators to each simulation, and in each case measured the mean bias $b = \langle \hat{p} \rangle - P_0$ for each pixel. The first column of Fig. 6 shows the bias of the naive estimator P^i . The second column shows the residual bias after using the modified asymptotic estimator (MAS). The biased regions in the SNR plane reduces considerably in comparison with the first column that has no correction. The third and fourth columns shows the residual bias using the known-angle estimator. As this estimator requires an independent value for the polarisation angle along with the observed values (Q', U') , we generated an additional $\times 10^5$ Gaussian realisations for the Q, U Stokes parameters of the template and with them, we reconstructed the known polarisation angle, centred at the true value, χ_0 , for each SNR value. Here, the SNR of the template is 2 (third column) and 3 (fourth column) times the SNR of the target.

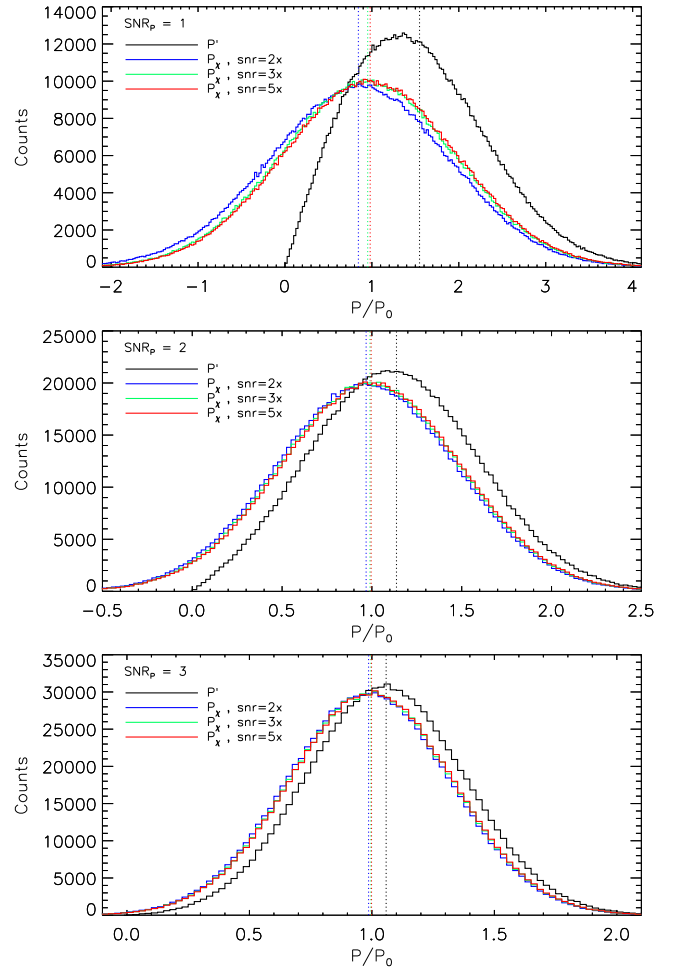


Figure 5. Histograms showing the distribution of \hat{p}_χ (coloured lines) and the naive (black line) estimator for three values of SNR in the target (top to bottom) and three values of the SNR of the template (as a multiple of the SNR of the target). All histograms are for the isotropic case, $\sigma_Q = \sigma_U$.

As expected, apart from numerical noise these results agree with the exact calculation shown in Fig. 3.

4.3 WMAP simulations

WMAP provided maps at five frequency bands between 23 and 94 GHz (Bennett et al. 2013). In the lower three frequencies the sky polarisation is dominated by Galactic synchrotron emission, with a brightness temperature that drops steeply with frequency ($T_V \propto \nu^\beta$, with $\beta \approx -3$). Since the brightness temperature sensitivity is similar in all bands, the highest SNR is at 23 GHz (K band), where large areas of diffuse polarised emission have $\text{SNR} > 3$ after smoothing to 1° FWHM resolution. In these bands the synchrotron polarisation angle reflects the Galactic magnetic field direction in the source regions, and is expected to be almost independent of frequency. The most likely cause of any frequency variation is superposition on the line of sight of regions with different field directions and also difference spectral indices β ; however, the variation of β for the synchrotron component is small as has been shown by Fuskeland et al. (2014) and (Vidal et al. 2015). On the other hand, the higher WMAP bands begin to be sensitive to dust polarisation, which has $\beta \approx +1.7$, and Planck data confirm that this

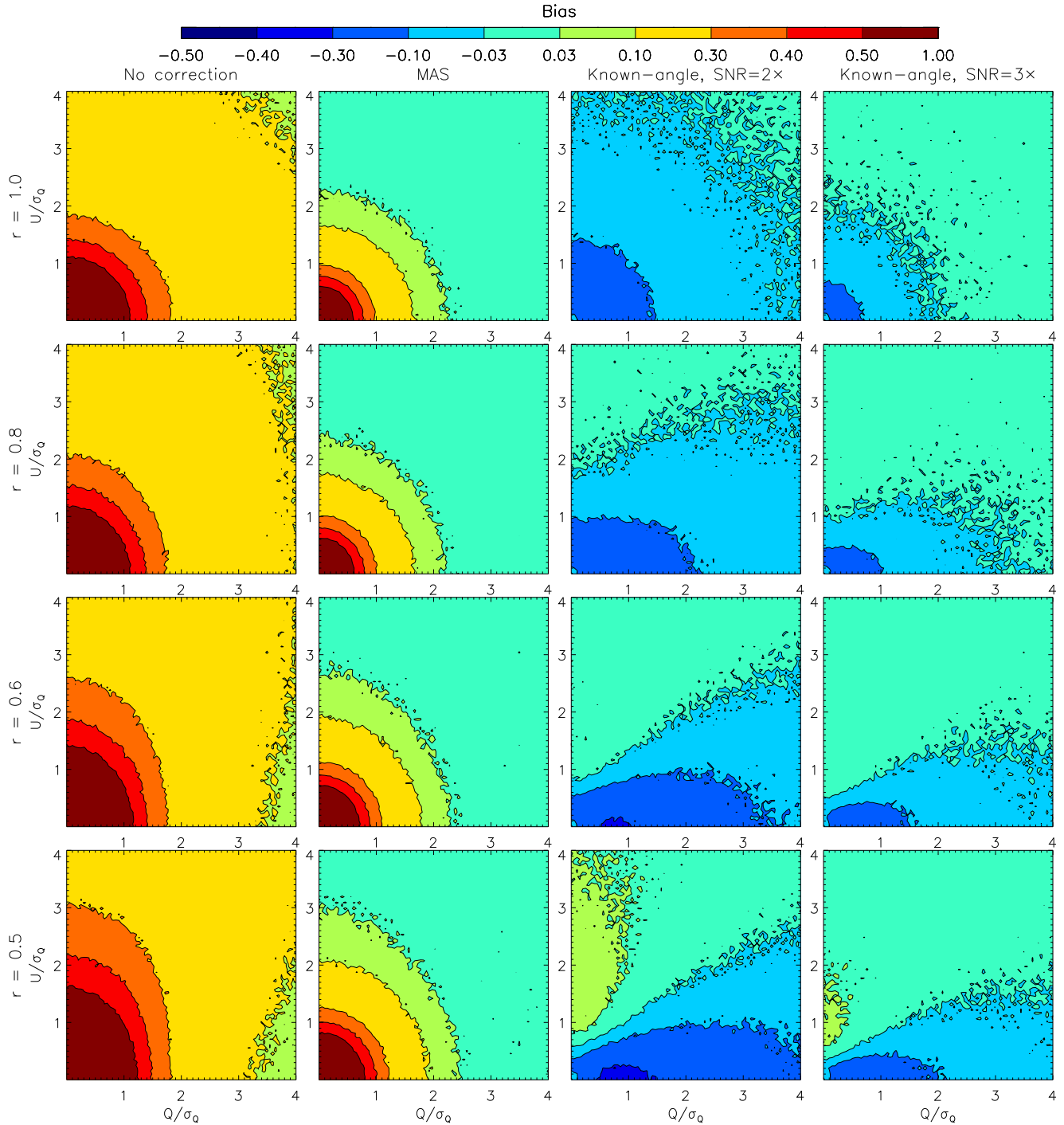


Figure 6. Contours of the mean residual bias of three estimators for the polarised intensity as a function of (Q, U) , calculated using Monte Carlo simulations for four different values of the error ellipse axial ratio, r . We take $\text{cov}_{QU} = 0$ (there is no loss of generality, as the covariance can always be eliminated by a rotation of the $Q-U$ axes). The colour scale represents the percentage bias of the estimated polarisation value in each pixel. The *left* column shows the naive estimator, \hat{p}' . The second column shows the MAS estimator, \hat{p}_{MAS} , from [Plaszczynski et al. \(2014\)](#). The third and fourth columns show the known-angle estimator, \hat{p}_χ , presented in Eq. 22 for two different SNR levels of the angle template: 2 times and 3 times the SNR of the target.

is generally significantly misaligned with synchrotron ([Planck Collaboration et al. 2015a,b](#)). For this reason we only consider the three lowest *WMAP* bands below.

Fig. 7 show histograms of the SNR for the Stokes parameters (Q, U) of the three frequency bands: K- (23 GHz), Ka- (33 GHz) and Q- (41 GHz) bands. The polarisation SNR in K-band is larger than the SNR in the other bands for almost the entire sky; in fact,

the SNR in the Ka-, and Q-bands rarely exceeds 3. In Fig. 8 we show histograms of the axial ratio of the error ellipses for all the pixels in these *WMAP* bands. The mean ratio for all the bands is $r = 0.86$.

We used the *Planck* Sky Model (PSM) ([Delabrouille et al. 2013](#)) to simulate the polarised sky at K-, Ka- and Q-bands at an angular resolution of 1° , from which we can obtain maps for the

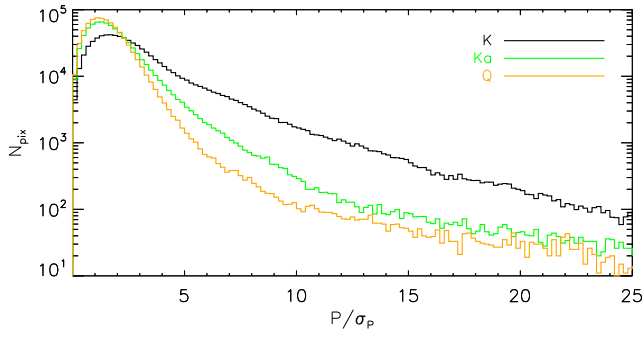


Figure 7. Histograms of the estimated signal-to-noise ratio of the polarisation amplitude, $\text{SNR}_P = P/\sigma_P$ of *WMAP* data in 3 frequency bands. The histograms are made using the full sky maps at an angular resolution of 1° , with $N_{\text{side}} = 256$. The percentage of pixels where the SNR at K-band is larger than the SNR at Ka and Q bands is 75% and 78% respectively.

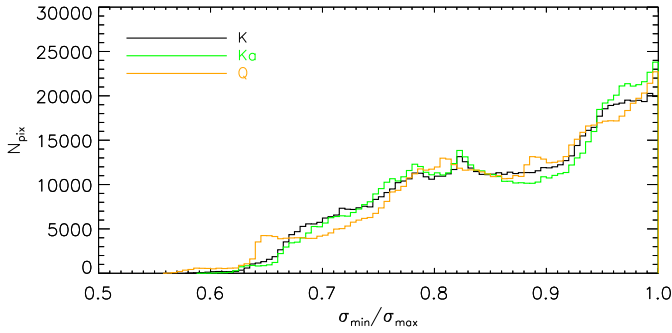


Figure 8. Histograms of the polarisation error ellipse axial ratio (Eq. 13) of *WMAP* data in 3 frequency bands. The histograms are made using the full sky maps at an angular resolution of 1° , with $N_{\text{side}} = 256$.

unbiased polarisation amplitude, P_0 . The model is closely based on the *WMAP* K-band map, and uses realistic spectral indices. We added random noise, generated using the *WMAP* covariance matrices C for each pixel, to the simulated Stokes Q and U map. The maps are generated at HEALPix $N_{\text{side}} = 512$. Smoothing was done by transforming to spherical harmonics, which were then divided by the window function of a Gaussian beam with 1° FWHM, then re-transformed. Noise and sky model maps were downgraded to $N_{\text{side}} = 64$ to give approximately independent pixels, and summed to give maps of the ‘observed’ polarisation amplitude, P' . In the top panel of Fig. 9 we show the reconstructed simulated polarisation angle map at K-band. The middle and lower panel of Fig. 9 show the observed polarisation angle by *WMAP* at Ka and Q-bands respectively. We can see that the simulated K-band angles, which we use as our template is very similar (but less noisy than) the observed angle at Ka and Q band. This is the characteristic that the known-angle estimator requires.

We corrected for the bias in these P' maps using the same three estimators discussed in Section 4.2. Ka- and Q-bands are corrected using the known-angle estimator where the angle information required by the \hat{p}_χ estimator is measured from the K-band map. We then compared these de-biased maps with the true polarisation amplitude map from the PSM simulations. In Table 1 we list the normalised bias value, averaged over the entire sky of 500 simulations for the three frequency bands that we studied.

The mean uncorrected bias, $\langle \Delta \hat{p}' \rangle = \langle P' - P_0 \rangle$ increases with

Table 1. Full-sky averaged values for the normalized polarisation bias and standard deviation of each estimator in simulated *WMAP* data, over 500 simulations. See Fig. 10 for the histograms of the errors $\hat{p} - P_0$.

Estimator	K-band		Ka-band		Q-band	
	$\langle \Delta \hat{p}' \rangle^a$	$\text{std}[\Delta \hat{p}]^b$	$\langle \Delta \hat{p}' \rangle^a$	$\text{std}[\Delta \hat{p}]^b$	$\langle \Delta \hat{p}' \rangle^a$	$\text{std}[\Delta \hat{p}]^b$
$\Delta \hat{p}'$	0.20	0.98	0.50	0.91	0.66	0.87
$\Delta \hat{p}_{\text{MAS}}$	0.06	1.00	0.27	0.93	0.42	0.88
$\Delta \hat{p}_\chi$	–	–	–0.05	1.01	–0.03	1.01

^a mean normalized bias, $\langle \hat{p} - P_0 \rangle / \langle \sigma_P \rangle$ where σ_P is given by Eq. 17.

^b Standard deviation of $\hat{p} - P_0$, again in units of the mean error.

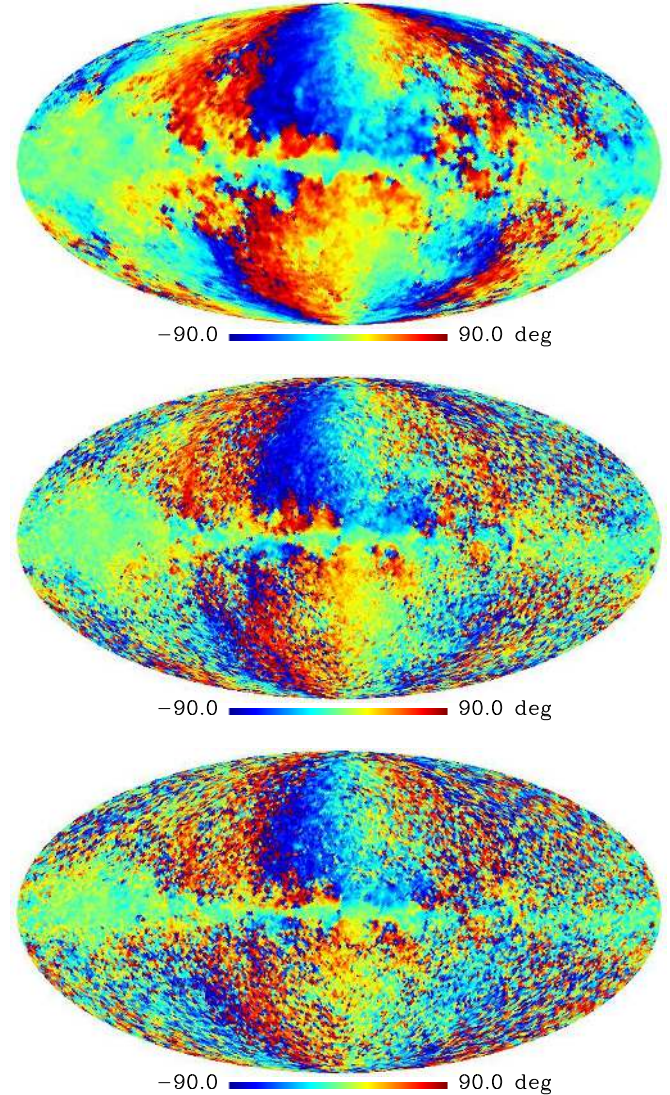


Figure 9. Full sky polarisation angle map. On *top* is the reconstructed angle map from the Planck Sky model with the added noise from *WMAP* K-band data. The *middle* and *bottom* panels show the observed polarisation angle from *WMAP* Ka and Q-bands respectively.

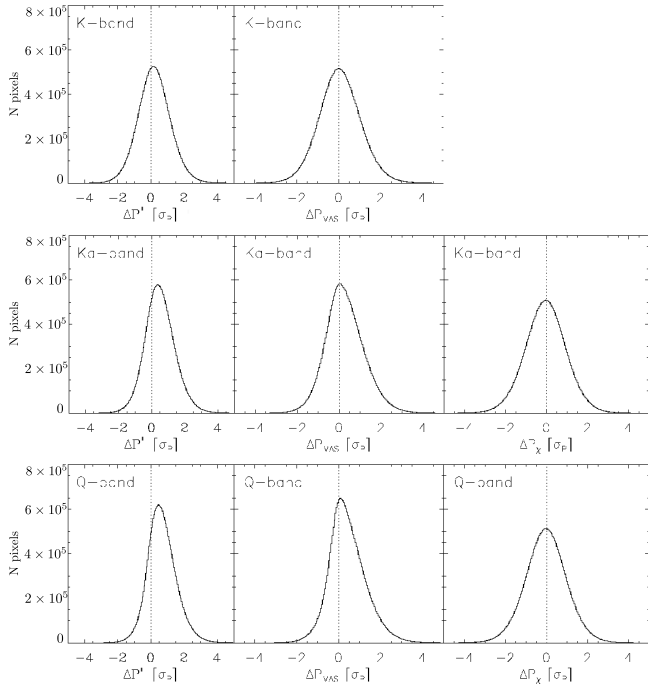


Figure 10. Histograms showing the bias of the three estimators studied for the simulated *WMAP* data at K, Ka and Q band described in the text. Histograms combine all 500 simulations and all sky pixels. They show the distribution of the difference between the estimators and the true polarisation amplitude P_0 , in units of the average polarisation noise, $\langle\sigma_P\rangle$. The column on the left shows the histograms of the polarisation bias of the naive estimator, i.e. the $\Delta P_0 = P' - P_0$ (no bias correction). The second column shows the residual bias for the MAS estimator, $\Delta P_{\text{MAS}} = \hat{p}_{\text{MAS}} - P_0$. For the noisier bands (Ka and Q), the histograms are not centred at zero, implying that there is additional residual bias on the corrected map. The third column shows the histograms produced using the \hat{p}_χ estimator, $\Delta P_\chi = \hat{p}_\chi - P_0$. Here the bias correction works much better and the distributions for the three bands are centred at zero. Table 1 lists the central values and spreads for all these histograms.

frequency due to the decrease in SNR. \hat{p}_{MAS} substantially reduce the bias at K and Ka bands, but Q band is so noisy that its impact is relatively modest. A clearer view of the effect of the estimators is revealed in the histograms of normalised errors, $P' - P_0 / \langle\sigma_P\rangle$, shown in Fig. 10. In Ka- and Q-band the histograms of the uncorrected polarisation maps are not centred at zero (the three plots in the left column). Where available, i.e. for Ka- and Q-bands, the \hat{p}_χ estimator performs dramatically better than \hat{p}_{MAS} . Note also that the histograms of the \hat{p}_χ estimator have a clear Gaussian shape. This shows that the uncertainty on the estimator (Eq. 23) can be used safely.

In order to see where the residual bias is more important, we show maps of the fractional bias after the correction using the different estimators. Fig. 11 shows the fractional bias at K-, Ka- and Q-band, for each of our estimators. Pixels where the residual bias is larger than 20 per cent are shown in grey. The \hat{p}_{MAS} estimator (second row) leaves a small residual bias over most of the sky (green areas in the Figure). The \hat{p}_χ estimator (bottom row) performs clearly better. In Table 2 we list the percentage of the area of the sky with a residual fractional bias smaller than ± 0.2 .

The excellent performance of the known-angle estimator in this case is due to the use of some extra information. The improvement is spectacular due to the very low SNR over much of the sky

Table 2. Percentage of the area of the full-sky map that have an absolute value of the residual fractional bias smaller than 0.2. These areas corresponds to the coloured pixels in Fig. 11.

Estimator	K-band %	Ka-band %	Q-band %
P'	84.9	35.0	18.4
\hat{p}_{MAS}	91.5	53.3	29.5
\hat{p}_χ	–	84.8	84.3

at the target frequencies. One could attempt to restore the signal-to-noise by simply smoothing to lower resolution, but this will fail when there is substantial real variation in the polarisation angle, which would cause the Q and U signals averaged over large areas to tend towards zero. The great advantage of the known-angle estimator is that we correctly preserve the true polarisation direction while still allowing coherent averaging of the polarised amplitude. Vidal et al. (2015) uses \hat{p}_χ to measure the spectral index of the diffuse synchrotron polarised emission over large regions of the sky, an ideal application of the known-angle estimator. It can also be applied in the *Planck* data, both for the low-frequency synchrotron emission and also for the high-frequency dust polarisation, where a natural template would be the highest available frequency, since the dust emission rises with frequency (Planck Collaboration et al. 2015b).

5 CONCLUSIONS

We have proposed a new way of correcting for the positive bias that affects the polarisation amplitude. The ‘known-angle estimator’, \hat{p}_χ , works when there is independent and high SNR information about the polarisation angle of the observed source. This additional information helps to reduce the polarisation amplitude bias.

We have derived formulae for the estimator, its precision, and its residual bias, due to the uncertainty in the template angle that is used. The estimator is continuous, analytic, possibly negative and highly Gaussian. Given an independent good template for the polarisation angle, i.e. the SNR of the template is at least two times the SNR of the target, this estimator performs excellently in the low SNR regime. We have shown with simulations using *WMAP* data that the known-angle estimator, \hat{p}_χ , outperforms the modified asymptotic (MAS) estimators, which is not surprise as \hat{p}_χ uses additional information about the U/Q ratio to correct for the bias. We believe that this new estimator will be of great use in datasets that encompass multiple frequencies with different SNR ratios like *Planck*, or even in multi-wavelength analysis mixing optical, infrared and radio data.

ACKNOWLEDGEMENTS

We thank the referee, S. Plaszczynski for very useful comments that have greatly improved the quality and presentation of this paper. We also thank Anthony Banday and Michael Keith for very useful comments on this work. MV acknowledges the funding from Becas Chile. CD acknowledges an STFC Advanced Fellowship, an EU Marie-Curie-IRG grant under the FP7 and ERC Starting Grant (no. 307209). We acknowledge the use of the Legacy Archive for Microwave Background Data Analysis (LAMBDA). Support for LAMBDA is provided by the NASA Office of Space Science. Some

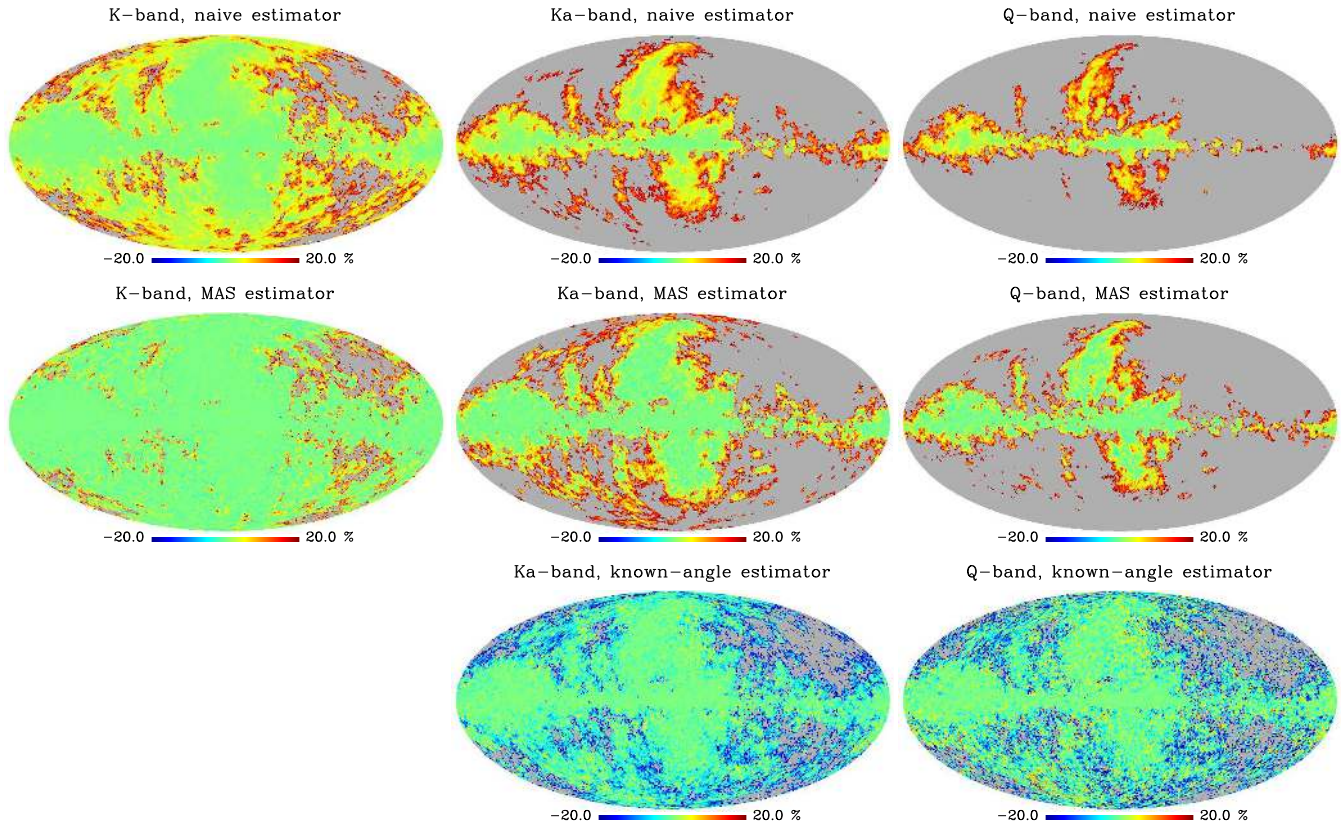


Figure 11. Maps showing the fractional bias in the *WMAP* K, Ka- and Q-bands (left, middle and right columns respectively). The top *top* row shows the fractional bias for the naive estimator $P' = \sqrt{Q'^2 + U'^2}$. The second row shows the residual bias when using the \hat{p}_{MAS} estimator and the *bottom* row has the residual bias that remains after correcting with the \hat{p}_{χ} estimator. All the pixels with an absolute value larger than 0.2 are shown in grey.

of the work of this paper was done using routines from the IDL Astronomy User's Library. Some of the results in this paper have been derived using the HEALPix (Górski et al. 2005) package.

REFERENCES

- Bennett C. L. et al., 2013, *ApJS*, 208, 20
 Delabrouille J. et al., 2013, *A&A*, 553, A96
 Fuskeland U., Wehus I. K., Eriksen H. K., Næss S. K., 2014, *ApJ*, 790, 104
 Górski K. M., Hivon E., Banday A. J., Wandelt B. D., Hansen F. K., Reinecke M., Bartelmann M., 2005, *ApJ*, 622, 759
 Kendal M., Stuart A., Ord J. K., 1994, *Kendall's Advanced theory of statistics. Vol. I: Distribution theory*
 Montier L., Plaszczyński S., Levrier F., Tristram M., Alina D., Ristorcelli I., Bernard J.-P., 2015a, *A&A*, 574, A135
 Montier L., Plaszczyński S., Levrier F., Tristram M., Alina D., Ristorcelli I., Bernard J.-P., Guillet V., 2015b, *A&A*, 574, A136
 Planck Collaboration et al., 2015a, *A&A*, 576, A104
 Planck Collaboration et al., 2014, *A&A*, 571, A1
 Planck Collaboration et al., 2015b, *A&A*, 576, A107
 Plaszczyński S., Montier L., Levrier F., Tristram M., 2014, *MNRAS*, 439, 4048
 Quinn J. L., 2012, *A&A*, 538, A65
 Rice S. O., 1945, *Bell Systems Tech. J.*, Volume 24, p. 46-156, 24, 46
 Serkowski K., 1958, *Acta. Astron.*, 8, 135
 Simmons J. F. L., Stewart B. G., 1985, *A&A*, 142, 100
 Vaillancourt J. E., 2006, *PASP*, 118, 1340
 Vidal M., Dickinson C., Davies R. D., Leahy J. P., 2015, *MNRAS*, 452, 656
 Vinokur M., 1965, *Annales d'Astrophysique*, 28, 412
 Wardle J. F. C., Kronberg P. P., 1974, *ApJ*, 194, 249

This paper has been typeset from a $\text{\TeX}/\text{\LaTeX}$ file prepared by the author.